

Structure and mechanical properties of carbon fibres: a review of recent microbeam diffraction studies with synchrotron radiation

Dieter Loidl,^{a*} Herwig Peterlik,^a Oskar Paris,^b Martin Müller,^c
Manfred Burghammer^d and Christian Riekell^d

^aInstitute of Materials Physics, University of Vienna, Boltzmannngasse 5, A-1090 Vienna, Austria,

^bDepartment of Biomaterials, Max-Planck-Institute of Colloids and Interfaces, Am Mühlenberg 1, D-14476 Potsdam-Golm, Germany, ^cInstitute of Experimental and Applied Physics, University of Kiel, Olshausenstrasse 40, D-24098 Kiel, Germany, and ^dEuropean Synchrotron Radiation Facility (ESRF), 6 rue Jules Horowitz, BP 220, F-38043 Grenoble CEDEX 9, France.

E-mail: loidl@ap.univie.ac.at

Hard X-ray beams with beam sizes in the sub-micrometre range are frequently available at third-generation synchrotron radiation sources, enabling new insights into the structure of materials at different levels of hierarchy by applying novel techniques such as scanning microbeam diffraction or scanning small-angle scattering. The high brilliance of the radiation from wiggler and undulator sources allows *in situ* experiments such as mechanical testing of single fibres to be performed, and even the combination of microbeam scanning with *in situ* testing is feasible. Three different experiments on single carbon fibres are presented: an *in situ* tensile test using a 10 µm collimated beam, a scanning experiment applying a 3 µm beam from a tapered glass capillary, and a scanning experiment with simultaneous *in situ* bending with a 0.1 µm beam provided by a waveguide structure.

Keywords: carbon fibres; glass capillary; waveguide.

1. Introduction

Carbon fibres are an ideal material for lightweight structures and are of particular importance for aerospace applications owing to their low weight, high tensile stress and high tensile modulus. Moreover, these extraordinary mechanical properties are maintained up to extremely high temperatures in vacuum or inert atmospheres (Loidl, Puchegger *et al.*, 2004). Although they were first experimentally applied in the late 19th century by Edison for incandescent lamps, the first commercial carbon fibres were not produced until the early 1960s (Young *et al.*, 1990). A number of different processing techniques as well as different precursor routes have been developed; the most important among them are based on polyacrylonitrile (PAN fibres), mesophase-pitch precursor (MPP fibres) and rayon [see Fitzer & Manocha (1998) for a comprehensive overview].

Many different methods have been applied to investigate the structure of carbon fibres, *e.g.* scanning electron microscopy (SEM) (Endo, 1988; Vezie & Adams, 1990; Kumar *et al.*, 1993; Huang & Young, 1994; Fortin *et al.*, 1995; Edie, 1998; Barnes *et al.*, 1998; Hong *et al.*, 1999), transmission electron microscopy (TEM) and high-resolution TEM (Diefendorf & Tokarsky, 1975; Bennett & Johnson, 1979; Bennett *et al.*, 1983;

Guigon *et al.*, 1984; Oberlin, 1984; Endo, 1988), as well as scattering methods (Perret & Ruland, 1970; Takaku & Shioya, 1990; Gallego & Edie, 2001). It was proposed (Takaku & Shioya, 1990; Fischer & Ruland, 1980) that PAN-based carbon fibres are built up of basic structural units (BSUs), which consist of ribbon-shaped layers of sp^2 -type graphene sheets. These BSUs are forming undulating microfibrils over a range of some hundreds of nanometres. Another model proposed crumpled and folded sheets of entangled layer planes, which are interlinked by their boundaries (Guigon *et al.*, 1984). The situation is still more complicated for MPP fibres owing to the variety of processing parameters (Ruland, 1990; Edie, 1998) and the number of observed textures, *e.g.* radial, radial-folded or onion-like [see Edie (1998) for recent review]. Even though carbon fibre research has now been in progress for more than four decades, there is still a lack of knowledge about many structural details, and their relation to the extraordinary mechanical properties is widely unknown. In particular, details about axial and cross-sectional textures such as skin-core structures are of outstanding interest from a fundamental as well as from an applied point of view.

Microfocus X-ray diffraction techniques using high-brilliance synchrotron radiation have been developed in recent years [see, for example, Riekell (2000) for a comprehensive

overview]. Several new optics have been introduced and successfully applied to produce X-ray microbeams, such as tapered glass capillaries (Engström & Riekkel, 1996), Fresnel zone plates (Suzuki *et al.*, 1997), Bragg–Fresnel lenses (Kuznetsov *et al.*, 1994), refractive lenses (Snigirev *et al.*, 1996; Lengeler *et al.*, 2002) and waveguide structures (Lagomarsino *et al.*, 1996; Cedola *et al.*, 1998). The use of a small beam for the investigation of carbon fibres has a number of advantages. The accuracy and reliability of preferred orientation determination is significantly enhanced when using single fibres, because in fibre bundles a tilt of fibres within the bundle cannot be separated from the tilt of the layers within the fibres (Paris *et al.*, 2002). The high brilliance of the radiation enables short exposure times allowing *in situ* experiments during loading of single fibres (Loidl *et al.*, 2003). Finally, scanning single fibres allows nanostructural parameters to be obtained as a function of position on the fibre (Paris *et al.*, 2000, 2001). The present work provides an overview on recent experiments on single carbon fibres by making use of the continuously decreasing size of microfocus X-ray beams.

2. Material and experimental

Different carbon fibres produced from polyacrylonitrile (PAN) and mesophase pitch (MPP) precursor were used for the investigations. The MPP fibres were chosen to cover a wide range of Young's modulus (see Table 1). The PAN-based fibres (HTA7, Tenax) were exposed to a high-temperature treatment (HTT) to obtain the same effect. Four different types of PAN fibres were used for the investigation: as received (HTA7-AR), HTA7-18, HTA7-21 and HTA7-24, with a HTT of 2073, 2373 and 2673 K, respectively.

All experiments were carried out at the microfocus beamline ID13 at the European Synchrotron Radiation Facility (ESRF) in Grenoble, France. A monochromatic X-ray beam with a wavelength of 0.0975 nm was used and diffraction images were recorded by an area detector (MAR CCD). Different focusing devices for obtaining an X-ray beam with considerable intensity and small diameter were used (Riekkel, 2000), *i.e.* a collimator (diameter $\sim 10\ \mu\text{m}$), a tapered glass capillary (diameter $\sim 3\ \mu\text{m}$) and a waveguide structure (diameter $\sim 0.1\ \mu\text{m}$). The respective experiments are discussed in the following sections.

A two-dimensional diffraction pattern obtained from a single carbon fibre is shown in Fig. 1. The 002 and 004 reflections originating from the stacking of the carbon layers, the 10 and the 11 band from the essentially two-dimensional crystal structure of the carbon layers, and the small-angle scattering (SAXS) signal from oriented pores are clearly visible. A number of different parameters describing the structure of carbon fibres can be obtained from such patterns. Here we focus on the 002 reflection (its spread in the azimuthal direction describing the orientation distribution of the graphene planes) and on the 10 band, from which the in-plane spacing of the C atoms within the graphene layers are obtained. One-dimensional radial or azimuthal scattering profiles were obtained by either azimuthally or radially aver-

Table 1

Some properties of the investigated fibres.

Fibre name and manufacturer	Type	Fibre diameter (μm)	Density (g cm^{-3}) [†]	Young's modulus (GPa)	002 HWHM ($^\circ$)
K321 (Mitsubishi)	MPP	10.48	1.9	136	17.6
E35 (DuPont)	MPP	9.7	2.10	197	12.0
E55 (DuPont)	MPP	10.18	2.10	358	7.09
FT500 (Tonen)	MPP	10.0	2.11	380	6.69
K137 (Mitsubishi)	MPP	9.54	2.12	500	3.42
HTA7-AR (Tenax)	PAN	6.84	1.77	198	19.0
HTA7-18 (Tenax)	PAN	7.3	1.77	273	16.3
HTA7-21 (Tenax)	PAN	6.44	1.78	332	11.8
HTA7-24 (Tenax)	PAN	6.2	1.91	349	9.64

[†] Data sheets

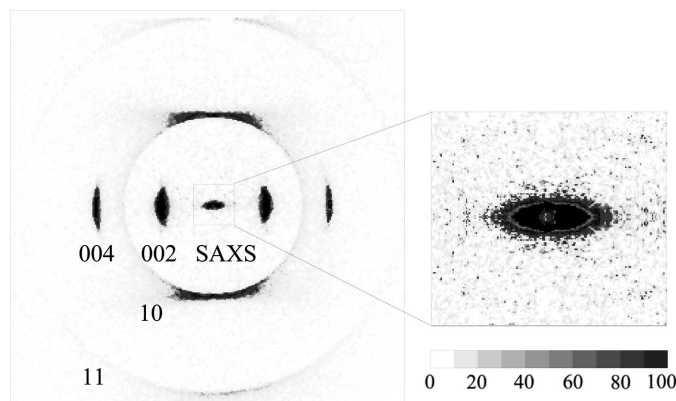


Figure 1

Two-dimensional scattering image from a single carbon fibre acquired using a MarCCD detector. A huge angular range of the scattering angle is covered ($0.85^\circ < 2\theta < 55^\circ$), allowing simultaneous collection of the SAXS signal with good resolution, as well as a large part of the WAXS signal. The different reflections are discussed in the text.

aging the corresponding regions in the two-dimensional images by using the software package *Fit2D* (Hammersley, 2005).

3. *In situ* tension experiments with 10 μm beam size

The diameter of the microbeam was defined by a 10 μm collimator to obtain a beam size slightly wider than the carbon fibres, which had a diameter ranging from 5 to 10 μm (Table 1). The high intensity of the beam allows the measurement of a diffraction image of one single carbon fibre with very good statistics within 30 s, and the background scattering from air is sufficiently low owing to the optimum beam size.

The single carbon fibres were glued into a sample holder and then tested in a stretching cell especially designed for *in situ* tension tests (Riekkel *et al.*, 1999). The load was increased stepwise to ensure constant stress conditions during recording of the diffraction image. This *in situ* experiment enables the measurement of the mechanical properties of the BSUs, *i.e.* of crystallites with a dimension of a few nanometres. The strain of the crystallites ε_{cr} in the axial direction can be obtained directly from the shift of the 10 band,

$$\varepsilon_{cr} = [d_{10}(\sigma) - d_{10}(0)]/d_{10}(0), \quad (1)$$

where d is the d -spacing derived from the position of the 10 peak and σ is the applied load. By integrating the 10 band only in a narrow sector in the meridional direction, the signal of only those crystallites which are perfectly aligned along the load axis of the fibre is used for the analysis. Values of Young's modulus of the nanocrystallites can thus be calculated by the derivative of the applied load σ with respect to the strain ε_{cr} ,

$$e_{cr} = d\sigma/d\varepsilon_{cr}. \quad (2)$$

To obtain an accurate value for the stress, the exact fibre diameter was determined by SEM, and a density correction using the crystallographic parameters together with the bulk density has to be performed to cope with the varying porosity of different carbon fibres (Loidl *et al.*, 2003).

Contrary to Young's modulus, the shear modulus g_{cr} can only be obtained indirectly from the decrease of the misalignment angle Π , which is given by the azimuthal width (half width at half-maximum, HWHM) of the 002 reflection. Theoretical models were developed to describe this unwrinkling of misoriented crystallites in dependence on the applied stress, see equation (3) (Northolt *et al.*, 1991; Shioya *et al.*, 1996),

$$\frac{d\Pi}{d\sigma} = -\frac{1}{2g_{cr}} \sin \Pi \cos \Pi. \quad (3)$$

Figs. 2 and 3 show the experimental results, from which the mechanical parameters of the nanocrystallites are obtained. Fig. 2 shows the change in d -spacing derived from the position of the 10 band by Braggs law, and Fig. 3 displays the misalignment angle in dependence on the tensile stress for all carbon fibres investigated.

Young's modulus and the shear modulus of the BSUs were obtained by applying (1)–(3) to the data shown in Figs. 2 and 3. Young's modulus, Fig. 4, increases significantly with decreasing misalignment angle (Loidl *et al.*, 2003; Loidl, Paris *et al.*, 2004). This can be interpreted by the crumpled

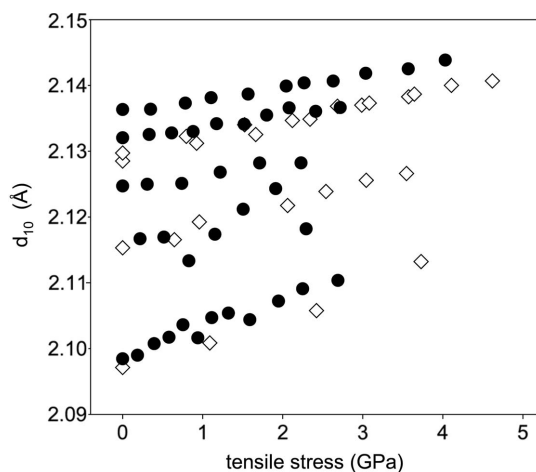


Figure 2 d -Spacing derived from the position of the 10 band in the fibre-axis direction in dependence on the applied tensile stress on the fibre. Filled symbols: MPP fibres; open symbols: PAN fibres.

arrangement of the graphene sheets, which also explains the fact that the fracture strain is higher for the fibres with higher HWHM. For the fibres with the smallest azimuthal width, a maximum value of 1140 ± 10 GPa is derived, which is clearly higher than the generally accepted value for single-crystalline graphite of 1020 ± 10 GPa (Blakslee *et al.*, 1970). It coincides, however, with the values of 1100 GPa obtained from static tests (Akita *et al.*, 1999) and 1200 ± 20 GPa from dynamic tests (Treacy *et al.*, 2000), published recently for carbon nanotubes. The small size of the BSUs in the nanometre range without the influence of defects or dislocations is probably the cause of these high Young's moduli. For the shear modulus, Fig. 5, a significant difference is visible between MPP fibres and PAN fibres (Loidl *et al.*, 2003; Loidl, Paris *et al.*, 2004). The reason for this is not yet clear; however, the higher value of the PAN fibres indicates the existence of covalent cross-links between the graphene layers of the BSUs. Another possible interpretation is given by a composite model for the fibre structure with a crystalline and an amorphous phase, which would also result in an increase in the shear modulus.

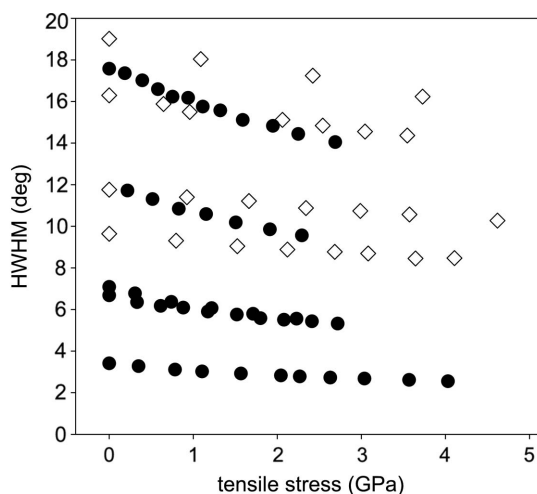


Figure 3 Azimuthal width (HWHM) of the 002 reflection in dependence on the applied tensile stress on the fibre. Filled symbols: MPP fibres; open symbols: PAN-fibres.

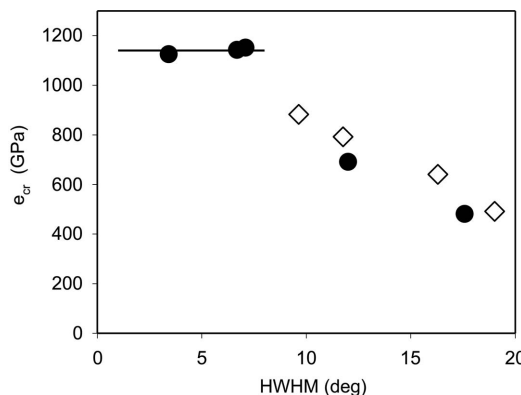


Figure 4 Young's modulus of the carbon nanocrystallites (BSUs) in dependence on the width of the 002 reflection. Filled symbols: MPP fibres; open symbols: PAN fibres.

4. Scanning experiments with 3 μm beam size

Focusing of the X-ray beam is possible by the use of a tapered glass capillary (Engström & Riekkel, 1996; Riekkel, 2000). This enables the scanning of small specimens with a position resolution in the micrometre range. To fully exploit the maximum position resolution, it is essential to determine the exact beam profile. A common approach is the scanning of the X-ray beam with a knife edge (we used a pinhole of 20 μm diameter), which is visible in Fig. 6 for two distances between the pinhole and the exit of the glass capillary. The left-hand figure shows the intensity curve and the calculated X-ray profile from deconvolution (using a step function for the pinhole with known diameter) at exactly the same distance, at which the specimens were measured (Paris *et al.*, 2001). The full width at half-maximum (FWHM) of the X-ray microbeam could thus be determined to be 3.11 μm . The right-hand diagram in Fig. 6 is obtained by increasing the pinhole–glass capillary distance by 1 mm. From the two values of the FWHM at different positions, the beam divergence can be estimated. Because of the high divergence, it is absolutely crucial to position the specimen as close to the capillary as possible. For the precise beam profile determination, it should be additionally taken into consideration that close to the edge the pinhole may not be completely opaque. A solution which overcomes this problem is the scanning of a carbon fibre with a

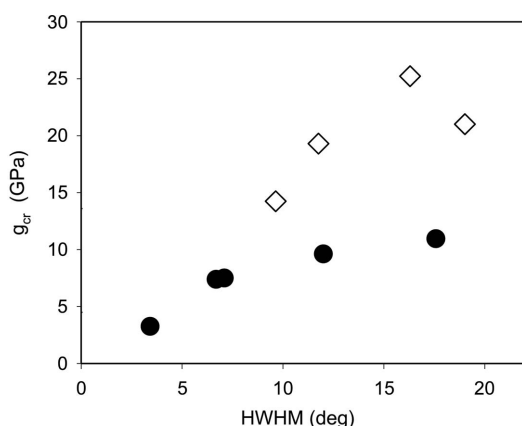


Figure 5
Shear modulus of the carbon nanocrystallites (BSUs) in dependence on the width of the 002 reflection. Filled symbols: MPP fibres; open symbols: PAN fibres.

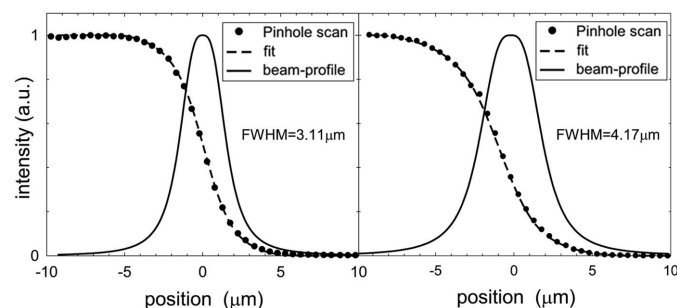


Figure 6
X-ray beam profile determination with a knife-edge scan. Left-hand figure: pinhole scan with fit and beam profile at the sample position; right-hand figure: distance increased by 1 mm. (From Paris *et al.*, 2001.)

precisely determined diameter (*e.g.* in a calibrated SEM) and with no cross-sectional texture. The total scattering intensity measured as a function of fibre position can then be deconvoluted with the volume function of the fibre. This is shown in Fig. 7, where simultaneously the intensity of the SAXS signal as well as the intensity of the 002 and 004 reflections were used for the deconvolution to obtain the beam profile with a FWHM of the microbeam of 3.08 μm (Paris *et al.*, 2001). The agreement with the pinhole scan is better than 1%.

Scanning of carbon fibres can be used to elucidate the axial and cross-sectional texture, which are both of critical influence for the mechanical properties. In Fig. 8, images of the fibres from (polarized) light microscopy and SEM on polished cross sections as well as SEM from corresponding fracture surfaces are presented. The image of the light microscope of the MPP fibre exhibits a faint birefringence effect as a consequence of the optical anisotropy made visible by polarized light, indicating a cross-sectional texture. The fracture surface of this type of fibre is furrowed, but the question is whether this is due to an inner structure or perhaps due to the complicated process of crack propagation during fracture (as for example in amorphous glass). Position-resolved scanning diffraction

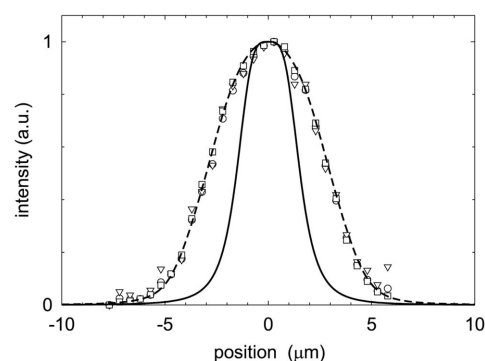


Figure 7
Beam profile determination by scanning a carbon fibre with no cross-sectional texture (PAN-based fibre HTA7). The beam profile is obtained by deconvolution with the fibre volume function. The different symbols correspond to the scattered intensity within different regions in the scattering pattern: 002, circles; 10, triangles; SAXS, squares. (From Paris *et al.*, 2001.)

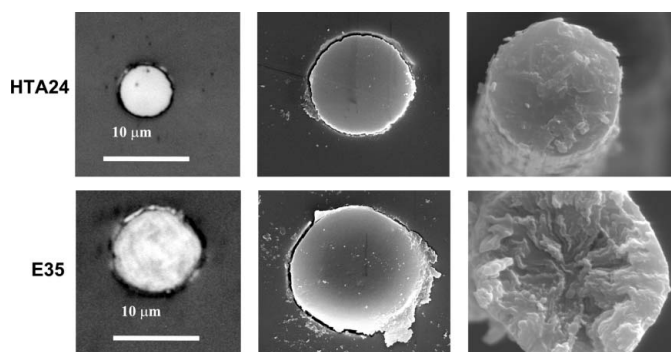


Figure 8
Microscopic images of fibre cross sections. Left column, polarized-light microscope images; centre column, the same fibre in the SEM; right-hand column, fracture surface of the same type of fibres.

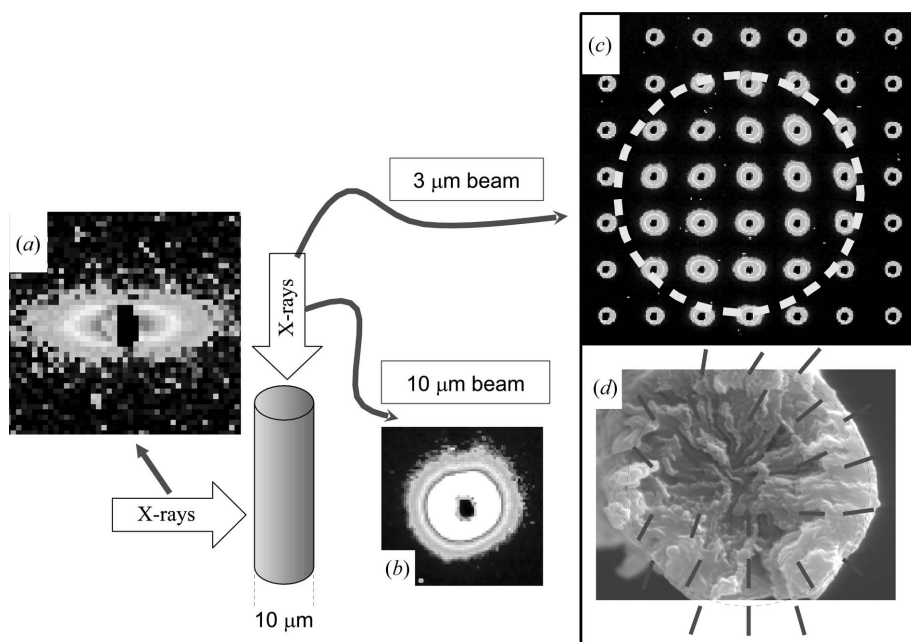


Figure 9

Two geometries for scanning SAXS and WAXS. (a) Fibre geometry: the beam is perpendicular to the fibre axis. (b) On-axis geometry: the beam is parallel to the fibre axis. (c) SAXS composite image from two-dimensional scanning of a thin slice of a carbon fibre in on-axis geometry. The anisotropy of the SAXS signal is directly related to the cross-sectional orientation of the shelf-shaped nanopores. (d) Cross-sectional pore orientation (direction of black lines) overlaid on the SEM image of the fracture surface of a MPP fibre.

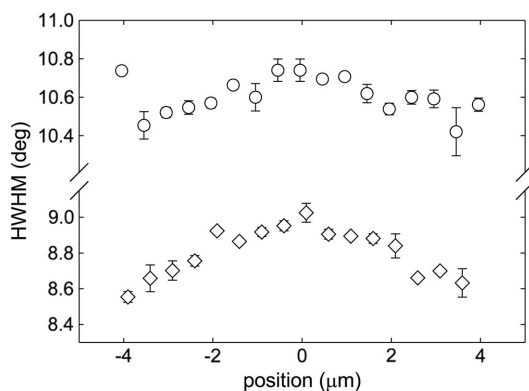


Figure 10

Scanning in fibre geometry. For HTA7-21 (HTT 2373 K, circles), the width of the 002 reflection is almost constant, whereas for HTA7-24 (HTT 2673 K, diamonds) a skin-core structure is clearly visible.

with an X-ray microbeam can be used to clarify this. In Fig. 9, two different geometries are outlined: (i) the on-axis geometry, from which directly a radially oriented structure is visible from the anisotropy of the SAXS signal within the fibre cross section (Paris *et al.*, 2000), and (ii) the fibre geometry, from which the axial texture is obtained.

One advantage of using a microbeam in connection with single fibres is the possibility of accurately determining the azimuthal width of the 002 reflection, which describes the axial preferred orientation of the carbon sheets. For comparison, significantly higher values were obtained using laboratory equipment on fibre bundles consisting typically of 6000 or 12000 single fibres. This is due to the inevitable additional

macroscopic tilt of the fibres within the bundle during processing and preparation (Paris *et al.*, 2002). A difference of about 3° seems to be small but, for highly oriented MPP fibres with a width around 5° , this is a considerable deviation from the true value.

The possibility of scanning in fibre geometry with a beam considerably smaller than the fibre diameter is advantageous for a closer insight into the structural details across the fibre. In Fig. 10 the position dependence of the 002 azimuthal width is shown for two PAN fibres. The smaller width close to the boundaries of the fibre HTA7-24 indicates a skin-core structure with the skin exhibiting a higher axial preferred orientation than the core. This effect is clearly smaller for HTA7-21, indicating a development of the skin-core structure with HTT. One must, however, be cautious with the interpretation of results from scanning in fibre geometry. An inverse skin-core effect (smaller width in the core) can not only be

caused by a higher axial preferred orientation of the core but also by a mixing of two phases with different cross-sectional texture (Paris *et al.*, 2002).

The condition for fulfilling Bragg's law for the 002 reflection and the 10 band for a radial orientation of the carbon sheets within the fibre cross section is depicted in the scheme in Fig. 11. A different position dependence of the two reflections is apparent, which can be used to obtain information about cross-sectional texture from the intensity ratio of the individual reflections as a function of position. Obviously the signal will be smeared for structures deviating from perfectly radial, such as for radially folded structures. If the exact beam profile as well as the fibre volume function are known, the amount of the folded phase and the degree of folding can be quantitatively determined in a two-phase model (Fig. 12, left-hand diagram) (Paris *et al.*, 2002). In contrast to the pitch-based fibres, a cross-sectional texture was not observed for the PAN fibres. In Fig. 12 (right-hand diagram) the intensities of the 002 reflection, the 10 band and the SAXS intensity coincide perfectly with the convolution of the beam profile with the volume function of the fibre.

5. Scanning combined with *in situ* bending using a $0.1 \mu\text{m}$ beam

A considerable improvement was the development of waveguide structures focusing the X-rays in one dimension to a size of about 100 nm (Lagomarsino *et al.*, 1996; Cedola *et al.*, 1998; Riekel, 2000). The second dimension is about $5 \mu\text{m}$, resulting in a line-shaped X-ray beam. Scanning experiments were simultaneously performed with different mechanical loading

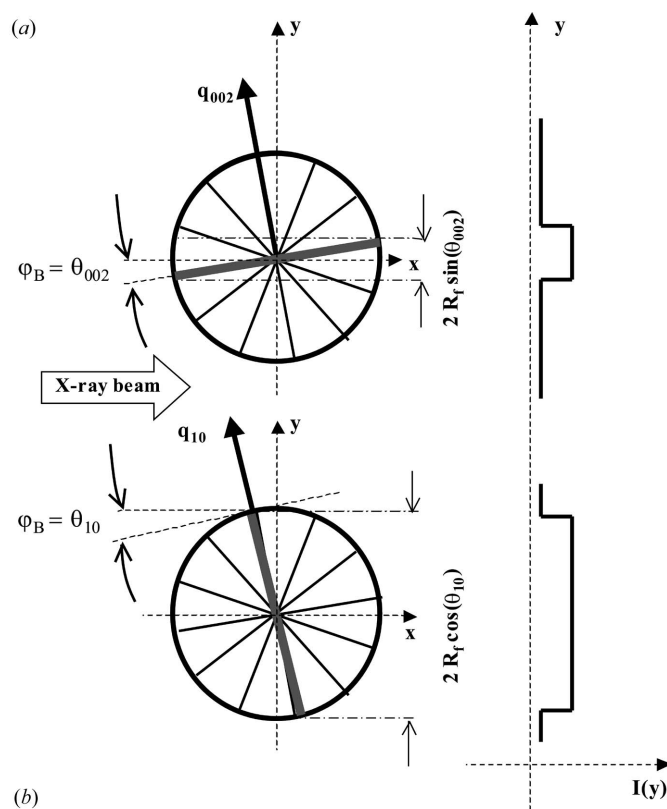


Figure 11

Sketch of the intensity distributions for a perfect radial orientation of carbon sheets scanned with an infinitely small X-ray beam. (a) 002 reflection, (b) 10 band. The Bragg condition is fulfilled for a wider range for the 10 band. (From Paris *et al.*, 2001.)

situations achieved by forming loops of carbon fibres with varying radii (Loidl *et al.*, 2005). To ensure the 100 nm resolution, the fibre had to be moved extremely close to the waveguide (a few μm), which was controlled with a light microscope from the top. Additionally, the long direction of the microbeam has to be perfectly aligned with respect to the fibre axis, which was achieved by moving the specimen in the beam until the 002 reflections were symmetric with respect to the waveguide plane. This procedure has a significantly higher precision in finding the top of the loop than using a light microscope for orientation. The fibres are then scanned starting from the tension zone at the top downwards to the neutral axis and then further to the compression zone.

Fig. 13 (left-hand diagram) shows that for the PAN-based fibre (HTA7-21) the integrated intensity of the 002 reflection perfectly follows the fibre volume function without the necessity of applying a convolution correction for the beam profile, necessary for the glass capillary. In Fig. 13 (right-hand diagram), the width of the 002 reflection is depicted. Whereas the axial preferred orientation is roughly constant across the fibre for the control experiment of the straight fibre, the orientation of the planes in the increasingly bent fibres differs significantly. The width decreases towards the tension zone (increasing tensile stress), and is more pronounced the smaller the bending radius. Towards the compressive zone, the width increases considerably. This is a clear indication of a buckling

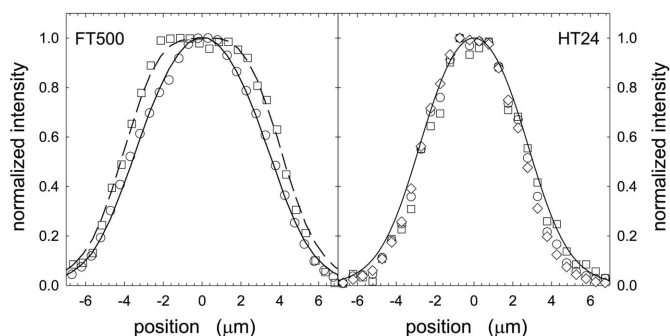


Figure 12

Cross-sectional texture from the position dependence of the equatorial intensity of the 002 and 10 reflections. Left-hand diagram: MPP fibre with different intensities for the 002 reflection (circles) and 10 band (squares). The lines are fit results from a two-phase model (random and radially folded phase). Right-hand diagram: PAN fibre with coinciding intensity values for the 002 reflection (circles), 10 band (squares) and SAXS intensity (diamonds). The full line shows the convolution of the fibre volume function with the beam profile. (From Paris *et al.*, 2001.)

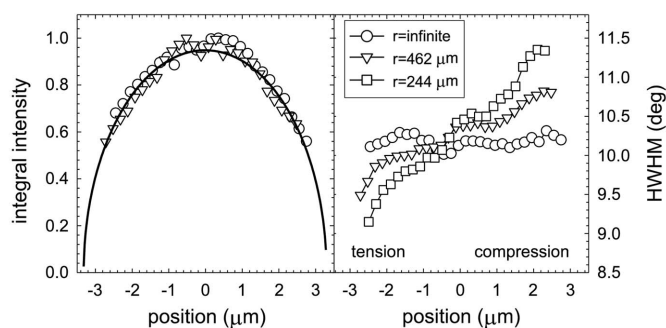


Figure 13

In situ scanning of bent PAN fibre. In the left-hand image the total intensities of the 002 reflection coincide with the volume function (no beam deconvolution required owing to the extremely small beam size). In the right-hand image the width is roughly constant for the straight (control) fibre, and shows a pronounced position dependence for the bent fibre. The effect increases with decreasing bending radius of the fibre (higher tension and compressive stresses).

of the graphene planes on a nanoscopic level, which has to our knowledge not been observed experimentally so far. A further interesting observation in Fig. 13 is that the neutral zone is shifted with respect to the geometrical centre of the fibre, which can be attributed to a different stiffness of the carbon fibre in tension and compression.

6. Conclusions

The recent developments in X-ray optics have lead to increasingly smaller beam sizes, enabling *in situ* scanning diffraction experiments on single carbon fibres. Applying mechanical load with simultaneous investigations of the atomic/molecular structure of single fibres with a position resolution down to the sub-micrometre regime has become feasible. The method has enormous potential. It is possible to obtain information on composition and structural changes of materials at the nanoscale and at the micrometre scale simultaneously. Examples were only shown here for carbon

fibres, but the ongoing synthesis and development of nanostructured materials offers a wide field of applications for X-ray microbeams, and the door has already been widely opened for X-ray nanobeams.

Support from the Austrian Science Funds, project no. P16315, is gratefully acknowledged. The waveguide was developed at the Budker Institute of Nuclear Physics (Novosibirsk, Russia) in the context of a collaboration with Sincrotrone Trieste (contact S. DiFonzo-Jark). We also acknowledge the allocation of beam time of the ESRF (proposals HS827, ME187 and ME368).

References

- Akita, S., Nishijima, H., Nakayama, Y., Tokumasu, F. & Takeyasu, K. (1999). *J. Phys. D.* **32**, 1044–1048.
- Barnes, A. B., Dauche, F. M., Gallego, N. C., Fain, C. C. & Thies, M. C. (1998). *Carbon*, **36**, 855–860.
- Bennett, S. C. & Johnson, D. J. (1979). *Carbon*, **17**, 25–39.
- Bennett, S. C., Johnson, D. J. & Johnson, W. J. (1983). *J. Mater. Sci.* **18**, 3337–3347.
- Blaklee, O. L., Proctor, D. G., Seldin, E. J., Spence, G. B. & Weng, T. J. (1970). *Appl. Phys.* **41**, 3373–3382.
- Cedola, A., Lagomarsino, S., Di Fonzo, S., Jark, W., Riekkel, C. & Deschamps, P. (1998). *J. Synchrotron Rad.* **5**, 17–22.
- Diefendorf, R. J. & Tokarsky, E. (1975). *Polym. Eng. Sci.* **15**, 150–159.
- Eddie, D. D. (1998). *Carbon*, **36**, 345–362.
- Endo, M. (1988). *J. Mater. Sci.* **23**, 598–605.
- Engström, P. & Riekkel, C. (1996). *J. Synchrotron Rad.* **3**, 97–100.
- Fischer, L. & Ruland, W. (1980). *Collect. Polym. Sci.* **258**, 917–922.
- Fitzer, E. & Manocha, L. M. (1998). *Carbon Reinforcements and Carbon–Carbon Composites*. Berlin: Springer.
- Fortin, F., Yoon, S. H., Korai, I. & Mochida, I. (1995). *J. Mater. Sci.* **30**, 4567–4583.
- Gallego, N. C. & Eddie, D. D. (2001). *Comput. Part A*, **32**, 1031–1038.
- Guigon, M., Oberlin, A. & Desarmot, G. (1984). *Fibre Sci. Technol.* **20**, 55–72.
- Hammersley, A. (2005). *The FIT2D Home Page*, <http://www.esrf.fr/computing/scientific/FIT2D/>.
- Hong, S. H., Korai, Y. & Mochida, I. (1999). *Carbon*, **3**, 917–930.
- Huang, Y. & Young, R. J. (1994). *J. Mater. Sci.* **29**, 4027–4036.
- Kumar, S., Anderson, D. P. & Crasto, A. S. (1993). *J. Mater. Sci.* **28**, 423–439.
- Kuznetsov, S. M., Snigireva, I. I., Snigirev, A. A., Engström, P. & Riekkel, C. (1994). *Appl. Phys. Lett.* **65**, 827–829.
- Lagomarsino, S., Jark, W., DiFonzo, S., Cedola, A., Mueller, B., Engström, P. & Riekkel, C. (1996). *J. App. Phys.* **79**, 4471–4473.
- Lengeler, B., Schroer, C. G., Benner, B., Gerhardus, A., Gunzler, T. F., Kuhlmann, M., Meyer, J. & Zimprich, C. (2002). *J. Synchrotron Rad.* **9**, 119–124.
- Loidl, D., Paris, O., Müller, M., Burghammer, M., Riekkel, C., Kromp, K. & Peterlik, H. (2004). *Nanotechnology in Construction*, edited by P. J. M. Bartos, J. J. Hughes, P. Trtik & W. Zhu, pp. 206–214. Cambridge: Royal Society of Chemistry.
- Loidl, D., Peterlik, H., Müller, M., Riekkel, C. & Paris, O. (2003). *Carbon*, **41**, 563–570.
- Loidl, D., Peterlik, H., Paris, O. & Burghammer, M. (2005). *ESRF Highlights 2004*, pp. 49–50. ESRF, Grenoble, France.
- Loidl, D., Puchegger, S., Kromp, K., Zeschky, J., Greil, P., Bourgeon, M. & Peterlik, H. (2004). *Adv. Eng. Mater.* **6**, 138–142.
- Northolt, M. G., Veldhuizen, L. H. & Jansen, H. (1991). *Carbon*, **29**, 1267–1279.
- Oberlin, A. (1984) *Carbon*, **22**, 521–541.
- Paris, O., Loidl, D., Müller, M., Lichtenegger, H. & Peterlik, H. (2001). *J. Appl. Cryst.* **34**, 473–479.
- Paris, O., Loidl, D. & Peterlik, H. (2002). *Carbon*, **40**, 551–555.
- Paris, O., Loidl, D., Peterlik, H., Müller, M., Lichtenegger, H. & Fratzi, P. (2000). *J. Appl. Cryst.* **33**, 695–699.
- Perret, R. & Ruland, W. (1970). *J. Appl. Cryst.* **3**, 525–532.
- Riekkel, C. (2000). *Rep. Prog. Phys.* **63**, 233–262.
- Riekkel, C., Dieing, T., Engström, P., Vincze, L., Martin, C. & Mahendrasingham, A. (1999). *Macromolecules*, **32**, 7859–7865.
- Ruland, W. (1990). *Adv. Mater.* **2**, 528–536.
- Shioya, M., Hayakawa, E. & Takaku, A. (1996). *J. Mater. Sci.* **31**, 4521–4532.
- Snigirev, A., Kohn, V., Snigireva, I. & Lengeler, B. (1996). *Nature (London)*, **384**, 49–51.
- Suzuki, Y., Kamijo, N., Tamura, S., Handa, K., Takeuchi, A., Yamamoto, S., Sugiyama, H., Ohsumi, K. & Ando, M. (1997). *J. Synchrotron Rad.* **4**, 60–63.
- Takaku, A. & Shioya, M. (1990). *J. Mater. Sci.* **25**, 4837–4879.
- Treacy, M. M. J., Krishnan, A. & Yianilos, P. N. (2000). *Microsc. Microanal.* **6**, 317–323.
- Vezie, D. L. & Adams, W. W. (1990). *J. Mater. Sci. Lett.* **9**, 883–887.
- Young, R. J., Day, R. J. & Zaikhani, M. (1990). *J. Mater. Sci.* **25**, 127–136.